

Low-Emittance Monoenergetic Electron and Ion Beams from Ultra- Intense Laser-Solid Interactions

*T. E. Cowan, M. Roth, M. M. Allen, J. Johnson, S. P.
Hatchett, G. P. Le Sage, S. C. Wilks*

This article was submitted to
2nd ICFA Beam Dynamics Workshop on the Physics of High
Brightness Beams, Los Angeles, CA., November 9-11, 1999

U.S. Department of Energy

Lawrence
Livermore
National
Laboratory

March 3, 2000

DISCLAIMER

This document was prepared as an account of work sponsored by an agency of the United States Government. Neither the United States Government nor the University of California nor any of their employees, makes any warranty, express or implied, or assumes any legal liability or responsibility for the accuracy, completeness, or usefulness of any information, apparatus, product, or process disclosed, or represents that its use would not infringe privately owned rights. Reference herein to any specific commercial product, process, or service by trade name, trademark, manufacturer, or otherwise, does not necessarily constitute or imply its endorsement, recommendation, or favoring by the United States Government or the University of California. The views and opinions of authors expressed herein do not necessarily state or reflect those of the United States Government or the University of California, and shall not be used for advertising or product endorsement purposes.

This is a preprint of a paper intended for publication in a journal or proceedings. Since changes may be made before publication, this preprint is made available with the understanding that it will not be cited or reproduced without the permission of the author.

This work was performed under the auspices of the United States Department of Energy by the University of California, Lawrence Livermore National Laboratory under contract No. W-7405-Eng-48.

This report has been reproduced directly from the best available copy.

Available electronically at <http://www.doc.gov/bridge>

Available for a processing fee to U.S. Department of Energy
And its contractors in paper from
U.S. Department of Energy
Office of Scientific and Technical Information
P.O. Box 62
Oak Ridge, TN 37831-0062
Telephone: (865) 576-8401
Facsimile: (865) 576-5728
E-mail: reports@adonis.osti.gov

Available for the sale to the public from
U.S. Department of Commerce
National Technical Information Service
5285 Port Royal Road
Springfield, VA 22161
Telephone: (800) 553-6847
Facsimile: (703) 605-6900
E-mail: orders@ntis.fedworld.gov
Online ordering: <http://www.ntis.gov/ordering.htm>

OR

Lawrence Livermore National Laboratory
Technical Information Department's Digital Library
<http://www.llnl.gov/tid/Library.html>

LOW-EMITTANCE MONOENERGETIC ELECTRON AND ION BEAMS FROM ULTRA-INTENSE LASER-SOLID INTERACTIONS

T.E. COWAN^{1,*}, M. ROTH^{1,2}, M.M. ALLEN¹, J. JOHNSON⁴, S.P. HATCHETT¹, G.P. LE
SAGE¹ AND S.C. WILKS¹

¹ *Physics Dept. L-280, University of California, Lawrence Livermore National Laboratory,
Livermore, CA 94550, USA*

² *Gesellschaft für Schwerionenforschung, Darmstadt, Germany*

³ *George C. Marshall Space Flight Center, Huntsville, AL 35812, USA*

E-mail: tcowan@llnl.gov

Recent experiments at the LLNL Petawatt Laser have demonstrated the generation of intense, high energy beams of electrons and ions from the interaction of ultra-intense laser light with solid targets. Focused laser intensities as high as 6×10^{20} W/cm² are achieved, at which point the quiver energies of the target electrons extend to ~ 10 MeV. In this new, fully relativistic regime of laser-plasma interactions, nuclear processes become important and nuclear techniques are required to diagnose the high-energy particle production. In recent experiments we have observed electrons accelerated to 100 MeV, up to 60 MeV bremsstrahlung generation, photo-nuclear fission and positron-electron pair creation. We also have observed monoenergetic jets of electrons having sufficiently small emittance to be interesting as a laser-accelerated beam, if the production mechanism could be understood and controlled. The huge flux of multi-MeV ponderomotively accelerated electrons produced in the laser-solid interaction is also observed to accelerate contaminant ions from the rear surface of the solid target up to 50 MeV. We describe spectroscopic measurements which reveal intense monoenergetic beam features in the proton energy spectrum. The total spectrum contains $>10^{13}$ protons, while the monoenergetic beam pulses contain ~ 1 nC of protons, and exhibits a longitudinal and transverse emittance smaller than conventional RF proton accelerator beams.

1 Introduction

The generation of highly relativistic laser plasmas has become possible in recent years with the advent of high power, chirped-pulse amplification (CPA) solid state lasers. The most advanced of these lasers is the Petawatt Laser [1] at Lawrence Livermore National Laboratory. The Petawatt uses one arm of the NOVA laser to amplify a frequency-chirped pulse to 800 J energies before temporal compression to ~450 fs. The peak power is well in excess of 1000 TW, and the beam can be focussed to a <10 μ m spot, with a typical intensity of 3×10^{20} W/cm². At these intensities the electromagnetic fields at the laser focus are $E > 10^{13}$ V/m, and $B > 10^5$ Tesla and the motion of the electrons in the target plasma is fully relativistic. The cycle-averaged oscillation or “quiver” energy of the electrons,

$$\overline{E} = mc^2 \left[1 + 2U_P / mc^2 \right]^{1/2} \quad (1)$$

can exceed several MeV, where $U_P = 9.33 \times 10^{-14} I (W/cm^2) \lambda^2 (\mu m)$ is the non-relativistic ponderomotive potential. The resulting distribution of electron energies in the target is predicted to resemble a Maxwellian [2], with mean energy given by Eq.1, and it extends far beyond the threshold for which nuclear effects become important.

On the face of the solid targets used in the present experiments a plasma was generated by a pre-pulse 2 ns before the main pulse and with an amplitude of $\sim 10^{-4}$ of the peak energy. The plasma served as a medium to self-focus the laser, thereby increasing the ponderomotive energy, and to produce electrons of even higher energy by a variety of laser acceleration mechanisms. The interaction of the electrons with the solid target produced high energy Bremsstrahlung, positron-electron pairs, and photo-nuclear reactions in the target material. Most recently, we have also observed the generation of very intense, directed beams of ions, produced at the rear surface of a target foil by ambipolar plasma expansion.

2 High-energy particle spectroscopy at the petawatt

To characterize the high-energy particles expelled from the Petawatt targets, we developed compact, permanent magnet spectrometers [3,4] as shown in Fig. 1. The spectrometers detect electrons, positrons and ions at energies between a few hundred keV and 100 MeV. They are mounted at 30°, 45° or 95° with respect to the laser beam direction and cover a very narrow angular range corresponding to a solid angle of $\sim 10^{-6}$ sr. The electrons and positrons are recorded in nuclear emulsion track detectors, which are positioned such that the particle angle of incidence is a constant value of 10° throughout the dispersion plane. The emulsions consists of two layers of 50 μ m thick, fine-grained silver bromide emulsion coated on the front and back

surface of a 500 μm polystyrene strip. Microscopic examination of the developed emulsion strips allows clear identification of charged particle tracks and, e.g., distinguishes electrons emitted from the target by virtue of the density of exposed grains along the track, the angle of incidence, and the transverse position along the emulsion strip. Ions are detected in an additional film pack which contained a nuclear emulsion strip and x-ray film [5].

The analysis of the tracks in the nuclear emulsion allows single particle detection without being overwhelmed by the blinding flash of x-rays from the laser plasma. Tracks of protons and heavy ions can be distinguished from those caused by minimum-ionizing positrons due to their higher specific energy deposition, which causes a thicker track in the emulsion. The spectrum of the particles is obtained by counting the number of individual tracks within a prescribed microscopic field of view and converting the track densities to absolute differential cross sections. The energy distribution (i.e. position versus energy) was calculated by ray-tracing and confirmed by measurements performed at the LLNL 100 MeV electron linac [6]. Above a certain particle density it is not possible to count single particles, because of the overlap of the individual tracks. Adding an x-ray film in front of the emulsion and analyzing the optical density in that film extends the sensitive range of the detector system.

The use of an x-ray film with a sensitive layer at both the front and back sides, in combination with the two active layers of the nuclear emulsion and the light-tight paper wrapper, effectively represents an energy discriminating multi-layer detector for protons and other ions. While the magnetic field of the spectrometer separates the momentum, the penetration depth of the particles in this detector reveals the energy signature of the particles. For a known particle species (e.g. protons), comparing the penetration depth of the particle with its momentum given by the position on the detector strip results in an additional and independent calibration method. Figure 2 illustrates this for energetic protons produced in Petawatt laser-solid interactions. The solid curve shows the expected proton kinetic energy based on magnetic deflection, calculated from the magnet field map (and consistent with direct electron momentum measurements on the electron linac). The data points indicate the energy expected for protons penetrating to the depth of a given active layer in the film detector, plotted versus the deflection position at which ion tracks are first observed in the given layer. The range-energy relation of the protons was calculated by TRIM simulations based on the known thickness and chemical composition of all the different layers in the detector. The correspondence of the range-energy calculation and the momentum measurement confirms that the vast majority of ions observed are protons. Although it is possible to distinguish other ion species by the range-energy method or by the specific ionizing rate along a given track, in practice this was difficult amongst huge flux of protons.

3 High energy electron generation and photo-nuclear reactions

As mentioned above, the interaction of the high intensity laser pulse with the preformed plasma on the face of a typical solid target, e.g., a 125 μm or a 2 mm Au foil, produces prodigious numbers of highly relativistic electrons. In addition, these electrons interact in the high-Z Au target material to produce hard Bremsstrahlung photons, which in turn drive a variety of photonuclear reactions. Figure 3a shows a direct measurement of the electron spectrum in one such shot, which exhibits electrons expelled in the forward direction at 30° with respect to the incident laser direction with energies of up to 100 MeV. The detailed shape of the spectrum, however, is expected to be significantly distorted, particularly for energies below the ponderomotive potential (several MeV) because of the time evolution of the space charge build-up at the target by the escaping high-energy electron current. We estimate that in typical high intensity Petawatt laser shots, the target can charge up to several MV in a time short compared to 100 fs.

In order to better understand the spectrum of laser-generated electrons, we have used photo-nuclear reaction yields to measure the hard Bremsstrahlung photons generated prior to the electrons escaping the potential well of the target. Bremsstrahlung photons above the threshold for photo-nuclear reactions produce long-lived radioactive daughter isotopes in the target [7-10]. After the laser shots, the targets were transported to a shielded high purity germanium gamma-ray spectrometer for time resolved measurements of the residual nuclear activation gamma rays to identify the isotopes produced by both the characteristic gamma-ray decay energies and their half-lives. Figure 3b compares the Bremsstrahlung spectrum predicted from the measured electron distribution, with that deduced from the measured yields of $^{197}\text{Au}(\gamma, \text{xn})^{197-x}\text{Au}$ reactions produced in the target material. These measurements directly demonstrate the generation of Bremsstrahlung x-rays above 60 MeV in these experiments. In addition, they suggest that the portion of the escaping electron spectrum above ~ 10 MeV is relatively unaffected by the target space-charge effects.

To complete our survey of photonuclear processes, we also encased 1.2g of ^{238}U within a copper sample holder on the back of the gold target on one Petawatt shot. After this shot we observed a large collection of additional gamma lines, including several that were previously detected from photo-neutron reactions in the Au and Cu target material [10]. The time-resolved spectroscopic data allowed us to identify many short-lived ray analysis was necessary to identify decay products from the photo-induced fission of ^{238}U . The nuclides we have identified by their gamma-ray line energies and half lives include $^{87,88}\text{Kr}$, $^{92,93}\text{Sr}$, $^{93,94,95}\text{Y}$, $^{101,104}\text{Tc}$, ^{105}Ru , ^{107}Rh , ^{128}Sb , ^{128}Sn , ^{134}Te , ^{135}I , ^{138}Xe , ^{138}Cs , ^{141}Ba and ^{146}Ce . The data were compared to previous measurements of yields for specific nuclides from photo-fission of ^{238}U with accelerator based Bremsstrahlung beams. As shown in Fig. 4, the mass distribution of the fission products lie upon the usual double-humped

distribution caused by the large deformation of the ^{238}U parent. The total yield in this experiment was estimated to be $(1.8 \pm 0.2) \times 10^7$ photo-fission events, $^{238}\text{U}(\gamma, f)$.

4 Positron creation

The nuclear emulsion track technique also proved to be ideally suited for the detection of very rare events, such as the production of positrons, because of its intrinsic single-particle detection sensitivity, and because of the relative immunity of emulsions to the high-energy x-ray flux generated in relativistic laser plasmas. The yield of positron-electron pairs in our experiments is expected to be of order 10^{-4} of the electron yield in the energy range 5-10 MeV. The sparse nature of the positron data required a complete microscopic scanning of the entire emulsion strip, with critical attention paid to the quality and characteristics of each track to avoid spurious misidentification of scattered background events. Previously, we found that the observed positron yield was consistent with pair production of Bremsstrahlung photons in thick targets [4]. Figure 5 shows the positron distribution for a thin, 125 μm Au target. The number of recorded positrons clearly exceeds the calculated yield expected for external pair conversion of Bremsstrahlung photons generated in the target.

Positron-electron pairs can also be produced by the Bethe-Heitler mechanism, that is the direct production in electron-ion collisions. Preliminary estimates of this so-called “trident” production, suggest a similar total yield as the Bremsstrahlung-component for these experimental parameters. If after further analysis of these data we ascertain that there is a statistically significant excess of positrons above the Bremsstrahlung and trident contributions, it could point to the direct production of electron-positron pairs by the violently quivering electrons in the laser plasma. This suggests that with future generation ultra-high intensity lasers, it might be possible to produce an actual relativistic pair plasma, in which the created positrons subsequently contribute to additional pair production via acceleration and collisions. This could have some relevance to astrophysical models of gamma-ray bursts or accretion disks, and in any case provide a terrestrial laboratory in which one could attempt to benchmark astrophysical relativistic plasma calculations. There may also be interesting Quantum Electrodynamics aspects, in terms of the suppression of the electron energy threshold for pair production because of the strong fields of the laser and plasma [11].

5 Electron Jets

In addition to the charged-particle spectroscopy and photo-nuclear activation measurements presented above, we also developed a large solid-angle, film-based range-filter detector to measure the spatial distribution of energetic particles accelerated in the intense laser-solid interactions [12]. Figure 6 shows a schematic

of the detector geometry. Disks of radiochromic film, interleaved with Ta foils of 100 – 600 μm thickness, were notched and rolled into a conical shape which subtended the forward angles up to nearly 90° with respect to the incident laser direction. Radiochromic film is sensitive to deposited energy, and hence has relatively low sensitivity to gamma-rays, higher sensitivity to minimum-ionizing electrons, and extremely high sensitivity to protons and other ions. By analysis of the energy deposition at different depths, total energy content and rough spectral information could be extracted for the electrons and ions observed leaving the rear surface, or penetrating the target foil. In particular, specific ion features could be discriminated from electrons by virtue of their very sharp energy deposition characteristics at the Bragg peak.

Figure 6 presents one example of a film exposure filtered by 600 μm of Ta. From systematic investigations of many shots, we can identify the many rather diffuse features as spatial isolated “jets” of electrons. As discussed below, the rather sharply defined feature at 0° can be associated with a beam of protons and other ions emitted predominantly from the back surface of the target foil [12]. The filter thickness corresponds to electron features above ~ 2 MeV. We interpret the spatial modulations of intensity as arising from filamentation of the laser beam as it propagates through the underdense blow-off plasma to the critical density surface, as well as of the ponderomotively driven electrons in the target which can form multiple, magnetically confined filaments of current in the solid density target. The existence of spatial modulation of the hard radiation patterns is also routinely observed in additional measurements of the variation of photonuclear activation yields in an array of gold pellets placed around the target [13]. Similar spatially isolated jets of electron current have been observed in a variety of other experiments, for example at the GEKKO laser facility at ILE-Osaka [14].

This spatial modulation of the electron filaments can affect the apparent reproducibility of the high energy electron yield, which we deduce from the magnetic spectrometer data. For very thick targets (several mm), multiple scattering of the electrons as they propagate through the target smears out the spatial distribution, and the measured spectrum appears to be quite a good representation of the average high energy electron flux (see, e.g., Figs. 3,4). For thin foil targets this correspondence can be problematic. For example, on some shots, we observe a very different spectral behavior for the electrons, which are emitted within the very narrow angular range of the magnetic spectrometer. Figure 6 (right) presents one such shot, in this case for a 5 ps pulse ($I \sim 3 \times 10^{19} \text{ W/cm}^2$) incident on a 1 mm thick CH target. Superimposed on the typical quasi-exponential spectrum, we observe a very intense, monoenergetic peak in the electron energy distribution at 15 MeV (with a width of 2 MeV, FWHM). On this particular shot, the radiochromic film image (not shown) exhibits a spatial filamentary structure which overlaps the angular acceptance of the magnetic spectrometer. We are presently working to correlate the large collection of shots on which we have recorded both electron energy spectra and spatial distributions, in order to ascertain whether there is a

physical correlation between the narrow electron “peaks” and the filamentary “jets”. If so, this suggests that this may be the first observation of *monoenergetic* laser-acceleration of plasma electrons. (Monoenergetic electrons have been observed in laser-gas target experiments in which atoms are ionized to a specific charge state at a specific laser intensity, which by conservation of canonical momentum results in a specific kinetic energy for the electron in vacuum [15].)

If we associate the monoenergetic feature with the spatial jet, we can evaluate the quality of this electron beam. The normalized rms emittance is then $<10 \pi$ mm-mrad, based on a predicted filament size of less than a few optical wavelengths and the measured angular distribution on the radiochromic film detector. The jet of Fig. 6 would then contain $>10^9$ electrons. However, the acceleration mechanism remains to be determined, and then one must evaluate whether it is possible to control the acceleration process and develop a reproducible, directional monoenergetic electron beam. At present, the occurrence of these monoenergetic jets is well established, but their specific energy and direction have not revealed a useful degree of reproducibility.

6 Ion acceleration

In addition to the diffuse electron filaments visible in the radiochromic film data, there are also very sharply defined regions of very high deposited energy which we understand to be a large flux of protons which are accelerated to several MeV in the Petawatt laser-solid interaction (see Fig. 7). This hypothesis was confirmed by including titanium foils in the radiochromic film/filter pack on a few shots, and by observing the production of radioactive ^{48}V by $^{48}\text{Ti}(p,n)^{48}\text{V}$ reactions. The pattern of activation closely matches the spatial distribution of intensity in the neighboring film layer [12]. An average proton energy could be deduced from the range-energy correlation from the film layers and was determined to be ~ 6 MeV. The total proton yield was determined from the total activation yield to be as high as 3×10^{13} protons per shot for a CH target. This corresponds to of order 30 J of energy transferred to fast protons, or up to 7% conversion efficiency of the 500 J laser pulse energy to fast ions.

We attempted to measure the ion energy spectrum directly in our magnetic spectrometer, but unfortunately the proton flux was so large as to saturate our emulsions and we could initially only determine the high energy end-point of the proton spectrum, as shown in Fig. 8. When the target was oriented normal to the line of sight of the spectrometer, that is, when the spectrometer viewed ions emitted normal to the target surface, we observe a high energy cut-off of typically ~ 50 MeV. As described above in Sec. 2, from the range-energy relationship in the multilayer film/emulsion detector, we determine that the overwhelming majority of ions at any given momentum are protons. We observe a lower cut-off energy, typically ~ 10 -15 MeV, when we detect protons emitted at 45° with respect to the

target normal. In subsequent experiments, we reduced the size of the entrance aperture to the spectrometer and were able to achieve improved dynamic range.

We also observed energetic protons when we irradiated metallic gold foils instead of CH targets. This suggests that the bulk of the accelerated ions come from contaminants on the target surface. This phenomenon of ionization and acceleration of target contaminants was seen many years ago in long pulse laser-solid interactions [16] in studies of ion ablation. Early spectroscopy studies [17,18] were able to detect protons and carbon ions of varying charge states. Recently, contaminant ions were also observed in short pulse high-intensity experiments using the Vulcan laser, where protons were accelerated into and through the target by the electron-ion charge separation at the forward driven critical density interface [19]. In contrast to the Vulcan laser, we had a relatively large and long time-scale pre-pulse on Petawatt, and we therefore expect that most of the contaminant hydrocarbons or water vapor would be ablated from the front surface of the target prior to the arrival of the high intensity laser pulse. This suggests that the bulk of the ions in our experiments actually were accelerated off of the rear, un-irradiated target surfaces. To test this, we irradiated a wedge-shaped target, oriented such that the front and rear target surfaces were not aligned. As shown in Fig. 9, we observe proton beams directed perpendicular to the two rear surfaces of the target.

Our understanding of the acceleration mechanism is a relativistic extension of the usual ambipolar expansion driven by the electric field in the sheath region of an expanding laser-plasma (see e.g., [20] and refs therein). This is further modified by the short-pulse, high intensity nature of the Petawatt laser conditions. The sequence is as follows. The pre-pulse level of the Petawatt first forms a ~ 50 - $100\ \mu\text{m}$ scale length plasma on the front surface of the target. The main pulse, having intensity of order $10^{20}\ \text{W}/\text{cm}^2$, then generates copious numbers of hot electrons having a characteristic "temperature" related to the ponderomotive potential, of several MeV. Many of these electrons leave the target, charging it to a multi-MV potential, which in turn draws most of the remaining electrons back to the target. The hot electrons oscillate through the target, and set up a plasma sheath at the front and rear surfaces of the target. At the rear, initially cold surface, the scale length of the sheath field is the electron debye length, of order a few microns. The typical hot electron density is $\sim 10^{19}\ \text{cm}^{-3}$ with a temperature of a few MeV. At the front surface, the electrons follow the scalelength of the pre-formed plasma, now $\sim 100\ \mu\text{m}$. The electric field in the plasma sheath on the rear of the target is of order $\text{MV}/\mu\text{m}$, which immediately field ionizes the low-Z contaminant atoms and begins to accelerate them very rapidly. Because the laser pulse is short compared to the acceleration time for the ions, the expansion is not isothermal (as for previous experiments [20]), and the electron temperature is reduced as the ion plasma expands because of the transfer of kinetic energy to the ions. Ions on the front, long-scalelength side of the target see a much reduced electric field and are accelerated much more slowly. Thus, as the hot electron distribution cools, and is neutralized by return currents in the target foil, the

ions at the rear of the target are much more violently accelerated and receive a larger share of the total energy from the hot electrons than those at the front surface.

This basic acceleration mechanism was first proposed by Gurevich [21], and was studied extensively, e.g. by Wickens and Allen [22], in regard to previous, long-pulse ion generation experiments. Almost all of these experiments dealt with ion acceleration off the irradiated surface by the laser-produced plasma. Recently, several groups working with high power short pulse lasers have observed ions accelerated into the target material [23], which arises from the charge separation as the electrons at the critical density surface are driven forward by the relativistic $\mathbf{v} \times \mathbf{B}$ force or by vacuum heating. The acceleration at the rear surface demonstrated in our experiments, is more consistent with the original Gurevich mechanism. In detailed spectroscopic measurements, we see many of the features one expects for the sheath-driven ion acceleration.

One interesting result of this plasma expansion, ion acceleration mechanism is that the different ion species in the expanding front segregate themselves because of their different charge to mass ratios. Anomalous “fast” ion generation was one of the early experimental results that drove much of the theoretical work. Wickens and Allen [22] and others [24] showed that segregation of the protons from carbon ions from CH targets should produce intensity modulations in the ion energy spectrum in multi-species and multiple electron temperature plasma expansions. We see similar results in our high resolution magnetic spectrometer data (i.e., with a small slit aperture to reduce the proton flux below the saturation limit in the emulsion and film detectors). Figures 10 and 11 show lineouts of the proton distribution from two shots on 125 μm Au foils (note that energy decreases with increasing magnetic deflection). Several very narrow proton features are apparent at the highest ion energies in these data. Figure 11 shows a deconvoluted proton energy spectrum from a rather smooth (least structured) shot. In addition to the broad distribution of protons extending up to nearly 30 MeV, we observe a narrow proton “peak” at 29 MeV, having a FWHM of 2 MeV. Several other shots show even more dramatic, isolated peak-like structures, and their analysis is in progress.

As is apparent from the radiochromic film data (Fig. 7), the angular divergence of the proton jet is rather well defined and decreases with increasing proton energy. This suggests that protons or other light ions accelerated from a surface by this mechanism may have a usefully small emittance in the sense of an actual particle beam. Moreover, the ion number appears to be large enough to be interesting for beam applications. For example, the rms divergence of the protons at 29 MeV is approximately 70 mrad, and the beam of Fig. 11 contains approximately 5×10^9 protons. The target size was 4 mm \times 4 mm, so the normalized rms emittance is certainly less than $\epsilon_{x,\text{rms}}^n < 70 \pi \text{ mm-mrad}$. By comparison, the typical normalized emittance in a proton linac, for example the 50 MeV “Linac2” injector for the CERN SPS, is $\epsilon_{x,\text{rms}}^n < 1.7 \pi \text{ mm-mrad}$.

To precisely estimate our emittance, we used penumbral imaging of the entrance slit of the magnetic spectrometer to directly measure the emittance of the

core of the proton beam. As shown in Figure 12, if we assume the proton beam is in a free drift region between the radiochromic film and the spectrometer, the entrance slit produces a sharp cut-off of the transverse spatial distribution, which is then smeared out as it propagates to the film plane in the spectrometer, according to the angular spread of the beam at the aperture. From fitting the beam profile in the nuclear emulsion film, we find that the angular spread at the collimator position is less than $\sigma_x \sim 2 \times 10^{-5}$ radian, at $x = 2.7$ mm. The image of the aperture on the emulsion detector projects back to a source point within a few 100 μm of the target foil position, so our approximation that the beam is freely drifting subsequent to acceleration appears reasonable. It should be emphasized that the proton beam is fully neutralized by the co-moving plasma electrons, so space charge expansion is not a concern until the electrons are separated from the ions as the plasma enters the magnetic spectrometer. This is confirmed by envelope calculations of the proton beam which show that at the observed beam current, neutralization must be nearly complete to obtain the observed small divergence.

The back-projected size of the apparent source based on the slit measurement would be $\sigma_x < 30$ μm . This is an unphysically small source size, if indeed the slit measurement views the entire source. Based on previous Petawatt experiments on electron generation, we expect that the electron distribution on the rear surface of the 125 μm thick Au target foil used in this shot would be much larger, ~ 300 μm , FWHM. The small apparent source size suggests that the acceleration process leads to a quasi-laminar beam, so that the initial phase space distribution already contains a great degree of correlation of emission angle with beam radius. We developed a two-dimensional extension of the 1-D Wickens and Allen style model to estimate the effect of radial fields on the initial plasma expansion. In particular, we calculated the effect of an initial gaussian radial distribution for the hot electron density on the rear surface of the target. The sheath field initially is proportional to the electron temperature divided by the electron debye length,

$$E_z \approx kT_{hot} \approx \sqrt{(N_{hot} \cdot T_{hot})} \quad (2)$$

which is largest at the center of the electron distribution. The ion front therefore accelerates more quickly at the center of the distribution, and during the first time step, advances further from the original target surface. This introduces a curvature in the ion front. If the sheath field is everywhere normal to the local ion front, then radial components of acceleration must be considered in future time steps. This evolves to a smoothly diverging radially symmetric beam in the cold ion limit. Using experimentally reasonable values for the initial hot electron temperature and density, the radius of the initial electron density distribution, and the time scale for the temperature depression of the electrons, leads to a laminar beam whose maximum divergence angle for a given proton energy closely matches the observed behavior pointed out in Fig. 7, that the proton beam is more highly focused for the highest proton energies. This radial expansion model has been confirmed in 2-D PIC simulations [25,26], as shown in Fig. 13 for an early-time snapshot of the

coordinate space and phase-space of ions accelerated off the back surface of a petawatt target.

The result of this analysis and modeling suggests that we observe a rather cold proton beam, which is smoothly diverging and highly laminar. The trace space of the highest energy protons exhibits a tilted ellipse, whose angular width is zero in the cold beam limit, but whose width ultimately is characteristic of the ion temperature. Our present upper limit on the proton temperature at the source is 5 keV, although this is limited by the resolution of our measurement from the slit data. We anticipate an ion temperature of order 100 eV, by electron-ion collisions in the expanding plasma front. At a temperature of 5 keV, we estimate the upper limit on our normalized rms transverse emittance to be $\epsilon_{x,rms}^n < 0.5 \pi$ mm-mrad, comparable or smaller than conventional RF linacs. (At 100 eV, $\epsilon_{x,rms}^n < 0.1 \pi$ mm-mrad.)

The occurrence of a small transverse emittance and a narrow proton energy spread represents in our opinion, the first observation of a truly accelerator-like beam from the laser acceleration of charged particles. The energy spread of order 10%, however, is still much larger than is conventionally achieved, so one might well question this assertion. However, because the acceleration process is driven by the strong fields in the debye sheath, which in turn depend critically on the high electron temperature and density (Eq. 2), the total duration of the ion acceleration is relatively short. In addition to giving their energy up to the accelerated ions, the hot electrons also lose energy by ionization energy loss in the target, and the density decreases as the radial flow of the electron distribution, both of which happen on the time scale of ~ 10 ps. We therefore expect the pulse duration of the protons to be initially quite short, also of order 10 ps. As a result, the longitudinal phase space area is similarly quite small, of order 10 keV-ns for a 2 MeV wide beam. This is small compared to RF linacs, suggesting that one may be able to manipulate the longitudinal phase space to advantage.

We have begun an effort to describe the proton plasma-expansion in usual beam coordinates, and can model the drift, focussing and injection of the Petawatt proton beam into a conventional accelerator. For example, by allowing for a ~ 0.5 m drift, the Petawatt proton beam becomes "energy-chirped" by simple velocity dispersion. This is sufficient to bunch it and inject it into a conventional drift tube linac structure. Although perhaps not an immediately interesting experiment, it demonstrates that the plasma-expansion acceleration from high intensity short pulse laser irradiation can produce ion beams of comparable quality as conventional RF accelerators.

As a final note on the potential interest in and application of this result, we can foresee a time when, with advances in solid-state laser technology it may be possible to have practical laser-ion injectors for which the injection energy is >10 MeV/amu, instead of ablation plasma injectors currently under development. This could replace the usual ion source, RFQ and first stage DTL linac at the beginning of a higher energy machine. More realistically, this type of ion source could be

used as a stand-alone compact accelerator, and opens a broad range of nuclear experiments to be performed with a table-top laser. One obvious application is to add charged particle ion beams to the tool-kit of ultrafast pump-probe experiments presently being performed in almost every short-pulse laser lab. Experiments such as studying the dynamic aspects of ion-induced materials damage will almost certainly be pursued within the next years. One might look further forward and consider whether table-top ion accelerators may open new uses in medicine and industry. For example, a future, compact, turn-key laser-based ion accelerator could enable new, shorter-lived radiopharmaceuticals for routine use in diagnostic or treatment regimens. Finally, one may consider very high energy density applications. For example, because the ion beam is generated as a neutralized plasma, it is not subject to the extreme space charge forces of non-neutralized beams, and can be ballistically focused to provide a very high energy density ignition driver for fast-ignitor Inertial Confinement Fusion (see Fig. 14, [27]).

7 Summary

We have observed a variety of phenomena which are new to laser-matter interaction science with the advent ultra-intense, 10^{20} W/cm² class Petawatt lasers. The electron motion in these laser fields is fully relativistic, and the generation of hard Bremsstrahlung, photonuclear reactions, and positron-electron pairs has been demonstrated. Narrow electron beam-like features are observed, but are at present not controllable. However reproducible, intense beams of protons can be produced. These have beam characteristics comparable to conventional ion accelerators, and may lead to a new field of compact laser-based ion acceleration research and development.

The author (T.E.C.) wishes to acknowledge many useful discussions with E. Esarey, T. Katsouleas, and Y. Sentoku, the expert technical support of W.S. Patterson, and the entire Petawatt experimental team (including C. Brown, M. Christl, E.A. Henry, W. Fountain, M. Key, A. MacKinnon, D. Pennington, T.C. Sangster, R.A. Snavely, M.A. Stoyer, Y. Takahashi and M.D. Perry). This work was performed under the auspices of the U.S. Dept. of Energy by the Lawrence Livermore National Laboratory under Contract W-7405-Eng-48.

References

1. M Perry *et al.*, Opt. Lett. **24** (1999) 160.
2. S.C. Wilks *et al.*, Phys. Rev. Lett. **69**, 1383 (1992).
3. T.E. Cowan *et al.*, in: Lasers '97, ed. J.J. Carroll (STS Press, McLean Va, 1998) 882.

4. T.E. Cowan *et al.*, in: Advanced Accelerator Concepts, ed. W. Lawson (AIP Conf. Proc. #472, 1998) 358; T.E. Cowan *et al.*, Laser Part. Beam 17, No. 4 (1999).
5. M. Roth, T.E. Cowan, J. Johnson *et al.*, to be published.
6. J. Johnson, M. Roth, T.E. Cowan *et al.*, to be published.
7. M.D. Perry *et al.*, Rev. Sci. Instrum. 70 (1999) 265.
8. M.H. Key *et al.*, Phys. Plasmas 5 (1998) 1966.
9. T.W. Phillips *et al.*, Rev. Sci. Instrum. 70 (1999) 1213.
10. T.E. Cowan *et al.*, Phys. Rev. Lett. **84**, 903 (2000). See also K. Leddingham *et al.*, Phys. Rev. Lett. **84**, 899 (2000).
11. K. MacDonald, private communication.
12. R.A. Snavely *et al.*, sub.to Phys. Rev. Lett. (Jan 2000).
13. M.A. Stoyer *et al.*, to be published.
14. Y. Sentoku *et al.*, Phys. Plasmas 6 (1999) 2855; R. Kodama *et al.*, Phys. Rev. Lett. **84**, 674 (2000).
15. A.J. Ting *et al.*, Phys. Rev. Lett. **83** (1999).
16. A.W. Linlor and W. Linlor, J. Appl. Phys. **44**, 4229 (1973).
17. C. Joshi, M.C. Richardson and G.D. Enright, Appl. Phys. Lett. **34**, 625 (1979).
18. R. Decoste and B.H. Ripin, Phys. Rev. Lett. **40**, 34 (1978).
19. E.L. Clark *et al.*, Phys. Rev. Lett. **84**, 670 (2000).
20. S J Gitomer *et al.* Phys Fluids, 29 (1986) 2679.
21. A.V. Gurevich, L.V. Pariiskaya and L.P. Pitaevskii, Sov. Phys. JETP **22**, 449 (1966).
22. L.M. Wickens and J.E. Allen, Phys. Fluids **24**, 1894 (1981).
23. G Pretzler *et al.* Phys.Rev.E. 58,1165(1998).
24. S. Sakabe *et al.*, Phys. Rev. A **26**, 2159 (1982).
25. Y. Sentoku, K. Mima, H. Habara, N. Izumi, R. Kodama, K.A. Tanaka and Y. Kitagawa, "Fast Ion Generation by Petawatt Laser Pulses under Oblique Incidence," ILE-OSAKA Preprint ILE9913TS.
26. S.C. Wilks, T.E. Cowan *et al.*, to be published.
27. M. Roth, T.E. Cowan *et al.*, "Fast ignition by intense laser-accelerated proton beams," sub. to Phys. Rev. Lett.

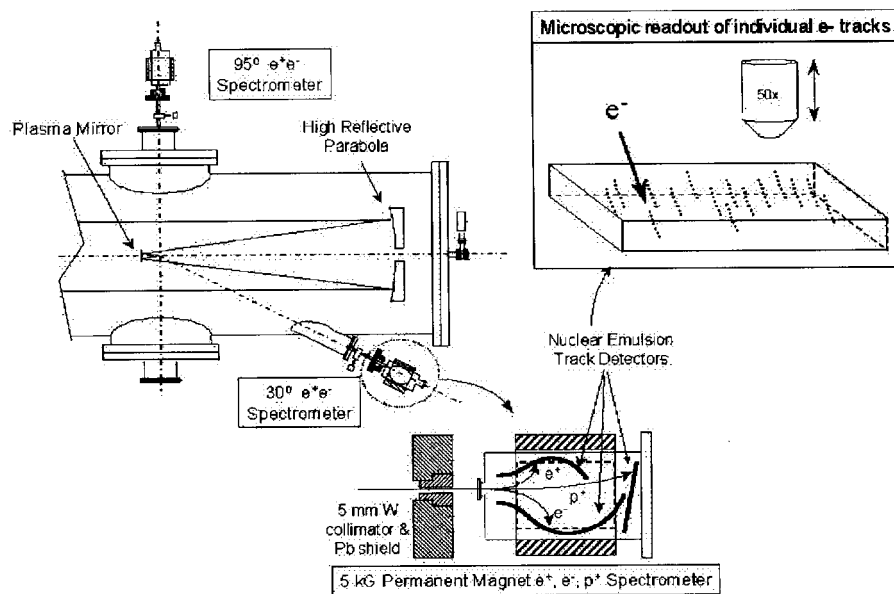


Figure 1. Schematic of the Petawatt target chamber and electron spectrometers. The laser beam enters from the left, is reflected from the parabola to a secondary plasma mirror, and reflected onto the target chamber center. The two spectrometers measure electrons (0.2 – 140 MeV), positrons (0.2 – 40 MeV) and ions (2 – 100 MeV) emitted at 30° and ~95° from the target.

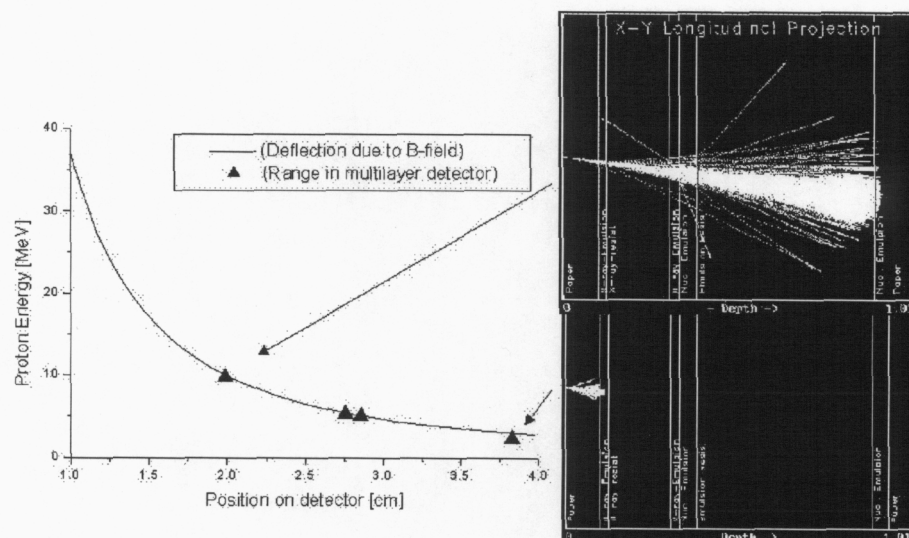


Figure 2. Proton energy versus position on emulsion detector. Solid curve calculated by ray-tracing. Data points plot the range-energy correlation for protons which penetrate to a given active layer in the emulsion/film detector stack (calculated with TRIM).

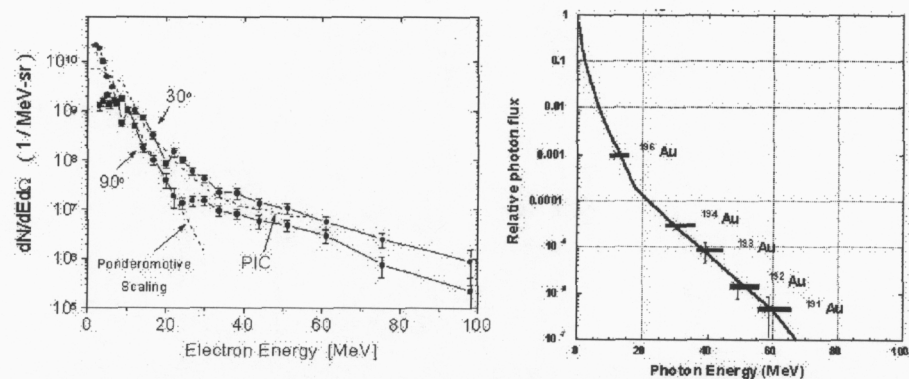


Figure 3. (Left) Measured energy distributions for electrons emitted at 30° and 90° with respect to the incident laser direction for a 300 J, 0.5 ps shot on thick gold targets. (Right) Calculated bremsstrahlung spectrum compared to yield of high energy photons determined from $^{197}\text{Au}(\gamma, xn)$ activation yields.

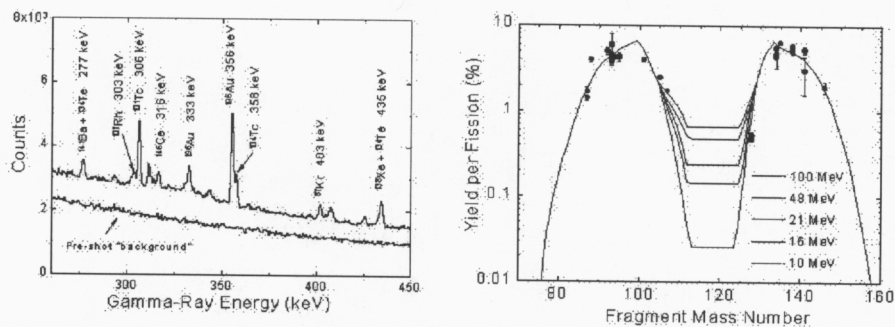


Figure 4. (Left) Spectrum of nuclear de-excitation gamma-rays emitted from target assembly during 4 hours after Petawatt shot. (right) Yield of fission fragments identified by gamma spectroscopy. The ^{238}U characteristic, "double-humped" mass distribution is clearly visible.

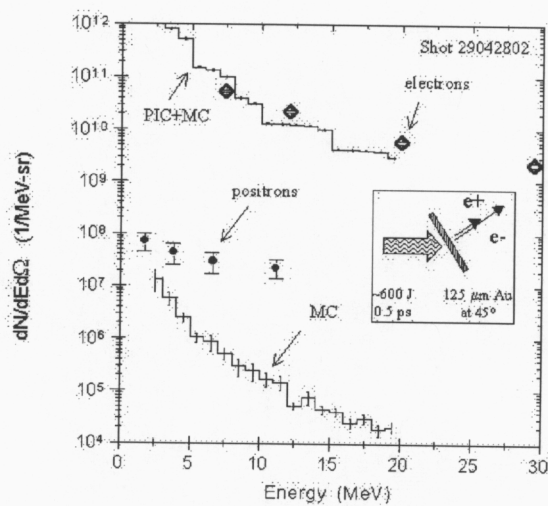


Figure 5. Spectra of electrons and positrons measured in 600 J/0.5 ps shot on 125 μm Au target. Histograms show PIC simulation of electrons, and corresponding prediction for positron creation by bremsstrahlung in the Au target.

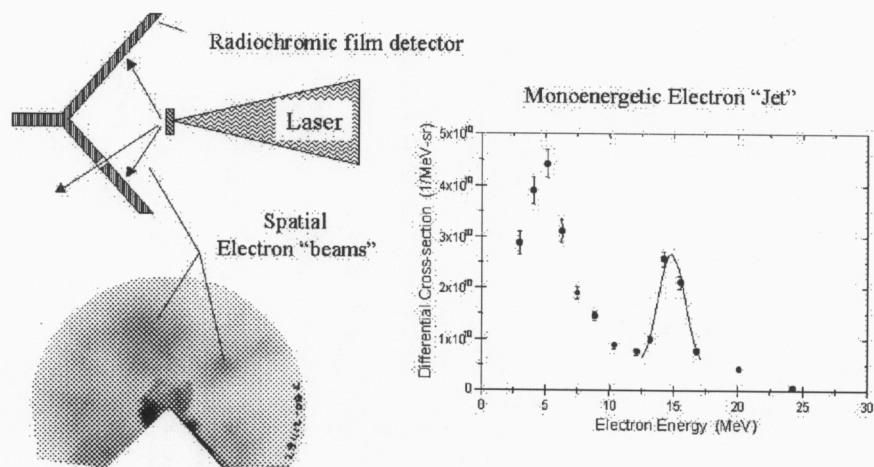


Figure 6. (Left) Spatial distribution of electrons >2 MeV determined by radiochromic film/filter detector. (Right) Spectral distribution of electrons in one filament, showing narrow, monoenergetic electron beam.

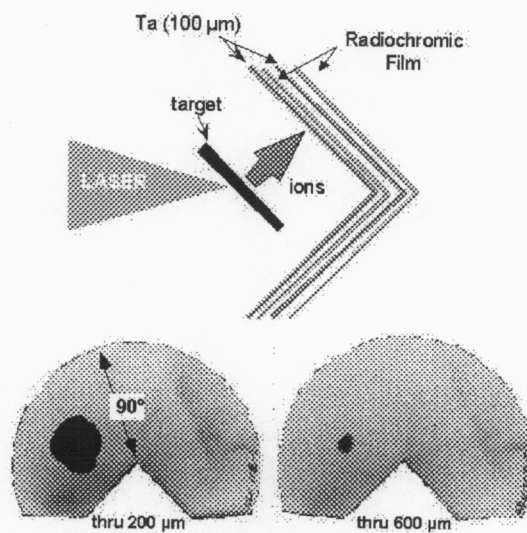


Figure 7. Spatial image of sharply defined proton beam feature emitted normal to the rear surface of the target foil, through two filter layers.

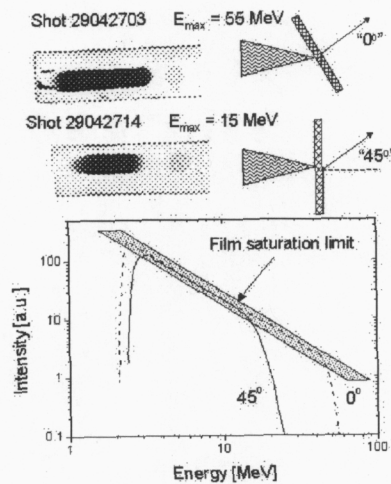


Figure 8. Images of the nuclear emulsion proton detector strips, and the respective proton energy distributions, for protons emitted at 0° or 45° to the normal to the target rear surface.

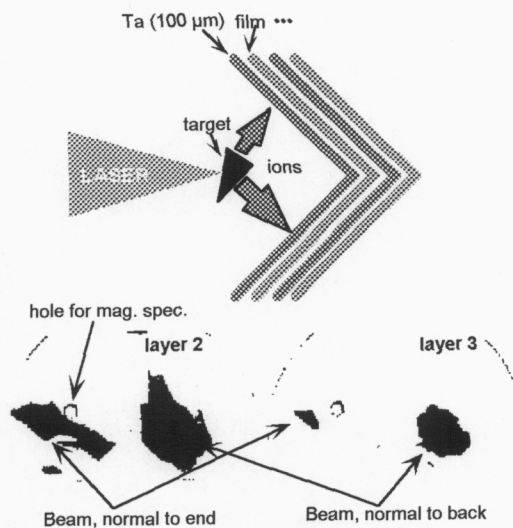


Figure 9. Radiochromic film images for shots on a 30° wedge shaped target. The most intense ion features correspond to emission perpendicular to the back and end of the target.

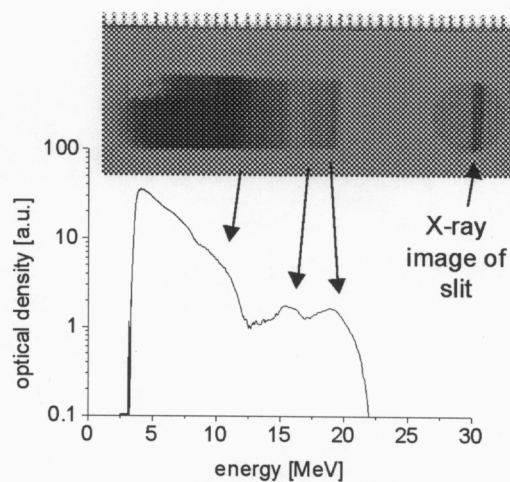


Figure 10. Film image and film lineout of 125 μm Au target shot. Multiple high energy structures are due to segregation and bunching of protons in the presence of different heavier ion species.

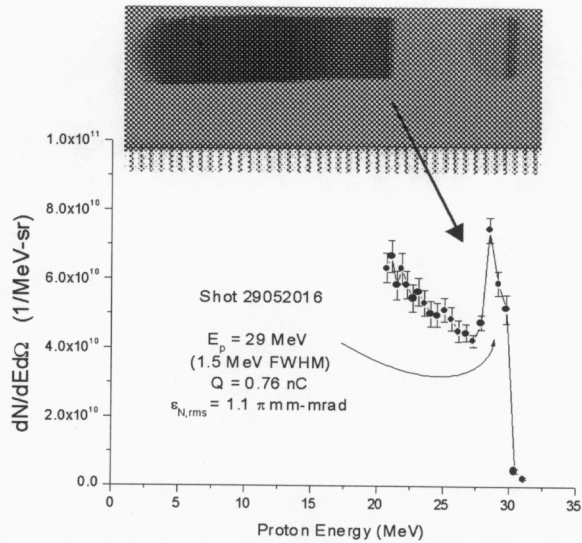


Figure 11. Film image and slit-deconvoluted lineout of shot 29052016 (125 μm Au foil). Lineout reveals narrow energy proton peak at 29 MeV, having 1.5 MeV FWHM, and containing 0.76 nC.

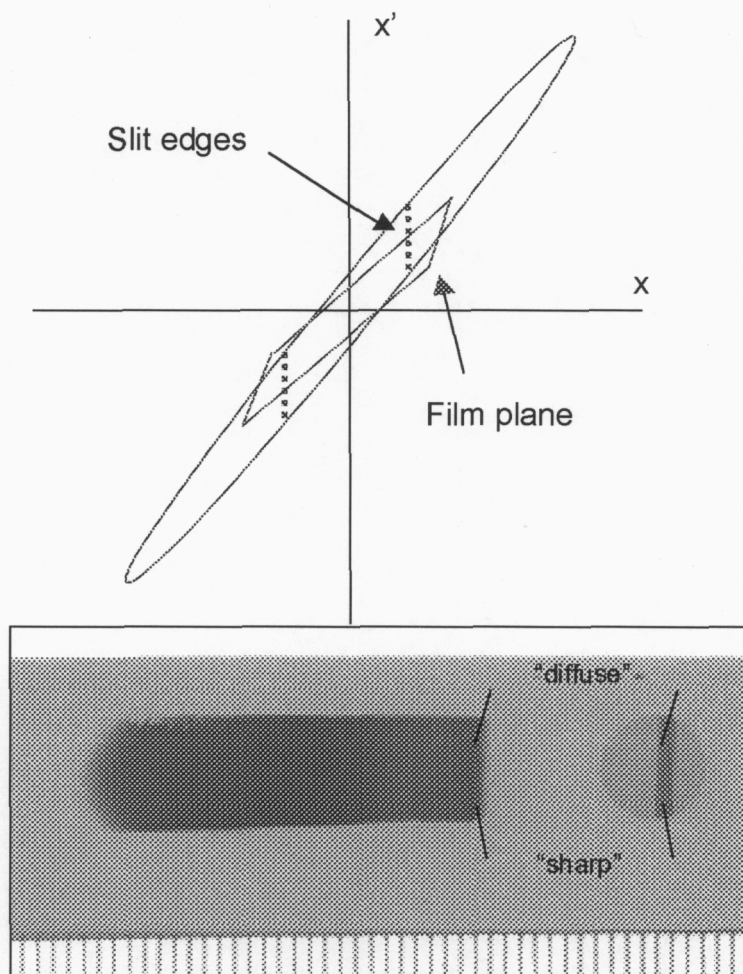


Figure 12. Trace space plot of proton beam transverse emittance ellipse at position of magnetic spectrometer entrance aperture. Note that the slit edge truncates the distribution. After drifting to the film plane, the edges of the proton image are spread according to the initial angular width of the distribution (top). Fits to the edge resolution imply an angular range $<20 \mu\text{rad}$.

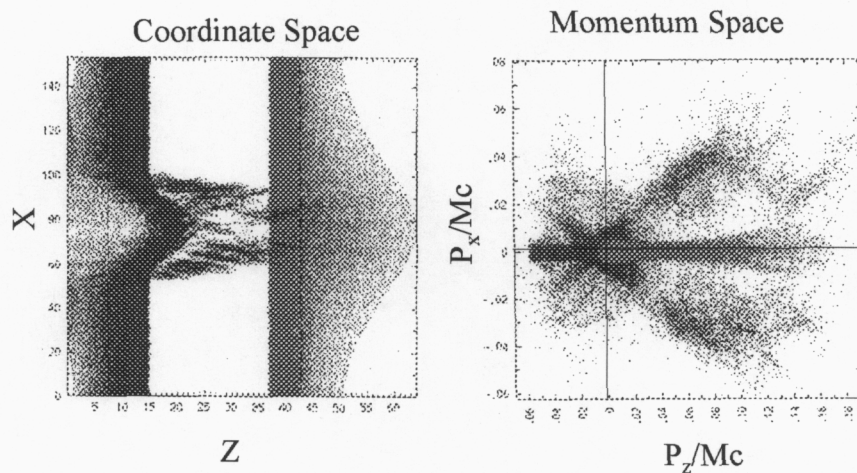


Figure 13. Two dimensional PIC simulation of the ion emission from the front and rear surface of a laser target. The coordinate space figure (left) shows the position of ions at ~200 fs after the laser pulse (laser enters from left). The dashed lines denote the original target surface. Note the expulsion of ions off of the front surface, acceleration of ions into the target, and the broad distribution of ions ions accelerated off of the rear surface (red). The momentum space plot (right) shows that the ions from the rear surface are accelerated into a narrow jet, having small divergence.

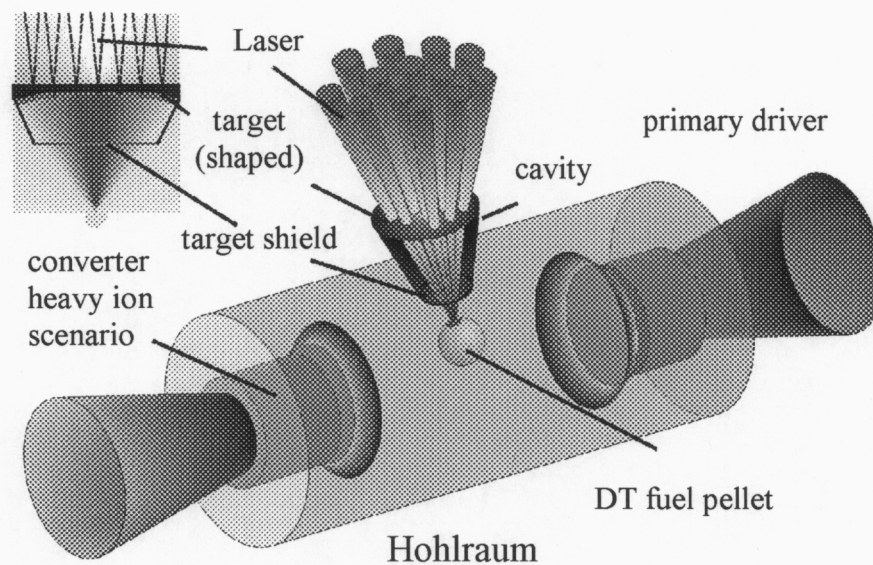


Figure 14. Schematic of ion-driven Fast Ignitor scheme for Inertial Confine Fusion. Heavy ion beams are shown entering the ends of the hohlraum to drive the initial fuel pellet compression. An multi-petawatt laser driven ion beam is shown, designed using ballistic focusing, to provide the initial heating to thermonuclear burn (see Ref. 27). Inset shows detail of spherically shaped proton target.